Pre- and post-stimulation characterization of geothermal well GRT-1, Rittershoffen, France: insights from acoustic image logs of hard fractured rock

Jeanne Vidal, Albert Genter, Jean Schmittbuhl

Geophysical Journal International

Geophys. J. Int. (2016) **206,** 845–860
Advance Access publication 2016 May 11
GJI Marine geosciences and applied geophysics

doi: 10.1093/gji/ggw181

Pre- and post-stimulation characterization of geothermal well GRT-1, Rittershoffen, France: insights from acoustic image logs of hard fractured rock

Jeanne Vidal,[1] Albert Genter[2] and Jean Schmittbuhl[1]

[1]*EOST, University of Strasbourg, 5 rue René Descartes, F-67000 Strasbourg, France. E-mail: j.vidal@unistra.fr*
[2]*ES-Géothermie, 3A Chemin du Gaz, F-67500 Haguenau, France*

Accepted 2016 May 9. Received 2016 May 9; in original form 2015 December 9

SUMMARY

Geothermal well GRT-1 (Rittershoffen, Alsace) was drilled in 2012. Its open-hole section (extending down to a depth of 2.6 km) penetrated fractured sandstones and granite. In 2013, the well was subjected to Thermal, Chemical and Hydraulic (TCH) stimulation, which improved the injectivity index fivefold. The goal of the study was to assess the impact of the stimulation by comparing pre- and post-stimulation well-logging (acoustic and temperature [*T*] logs) and mud-logging data. This comparison revealed modifications of almost all the natural fractures. However, not all of these fractures are associated with permeability enhancement, and the post-stimulation *T* logs are important for characterizing this enhancement. Chemical alteration due to mechanical erosion at the tops and bottoms of the fractures was observed in the sandstones. These zones display indications of very small new permeability after the TCH stimulation. Because a major fault zone caved extensively where it crosses the borehole, it was not imaged in the acoustic logs. However, this originally permeable zone was enhanced as demonstrated by the *T* logs. Based on the natural injectivity of this fault zone, hydraulic erosion and thermal microcracking of its internal quartz veins are associated with this permeability enhancement. Although local changes in the borehole wall observed in the acoustic images cannot be directly linked to the improved injectivity index, the comparison of the acoustic image logs allows for identification of fracture zones impacted by the TCH stimulation.

Key words: Downhole methods; Hydrothermal systems; Permeability and porosity; Fracture and flow; Fractures and faults; Europe.

INTRODUCTION

In the Upper Rhine Graben (URG), several deep geothermal projects, such as those in Soultz-sous-Forêts, Landau and Insheim, exploit local geothermal reservoirs trapped in the fracture network in Triassic sediments and the underlying granitic basement (Genter *et al.* 2000; Baumgärtner & Lerch 2013; Hettkamp *et al.* 2013). These projects are based on the Enhanced Geothermal System (EGS) technology. The principle underlying this technology consists of increasing the low initial natural hydraulic performance of pre-existing natural fractures in the geothermal reservoir via hydraulic and/or chemical stimulation (Schulte *et al.* 2010).

An EGS project located at Rittershoffen (Alsace, France) was initiated in 2011 by the company ECOGI, a partnership between the companies Groupe Electricité de Strasbourg and Roquette Frères and the French public financial institution La Caisse des Dépôts et Consignation. The project is based on a geothermal doublet that produces geothermal heat from the reservoir at the sediment-basement interface (Baujard *et al.* 2015). The heat will be used for industrial processes at the Roquette Frères biorefinery at Beinheim, located 15 km west of the drill site. The first vertical geothermal well, well GRT-1, was drilled to a depth of approximately 2.6 km in 2012. The open-hole section penetrated fractured Triassic sandstones, Palaeozoic hydrothermally altered granite and fresh granite. After hydraulic testing, the injectivity was insufficient for future industrial exploitation, and the well was therefore Thermally, Chemically and Hydraulically (TCH) stimulated in 2013. After the TCH treatments, the injectivity of well GRT-1 increased fivefold.

To identify the physicochemical processes responsible for this hydraulic improvement, we compared pre- and post-stimulation data sets obtained from well GRT-1. In this paper, first, the geologic setting and the TCH stimulation operations at the Rittershoffen site are presented. Then, methods used to compare the pre- and post-acoustic image logs and to correlate observations in these logs and indications of permeability based on temperature profiles are described. Last, the results regarding post-stimulation modified fracture zones and permeability enhancement in the well are discussed. On the whole, the stimulation is generating only

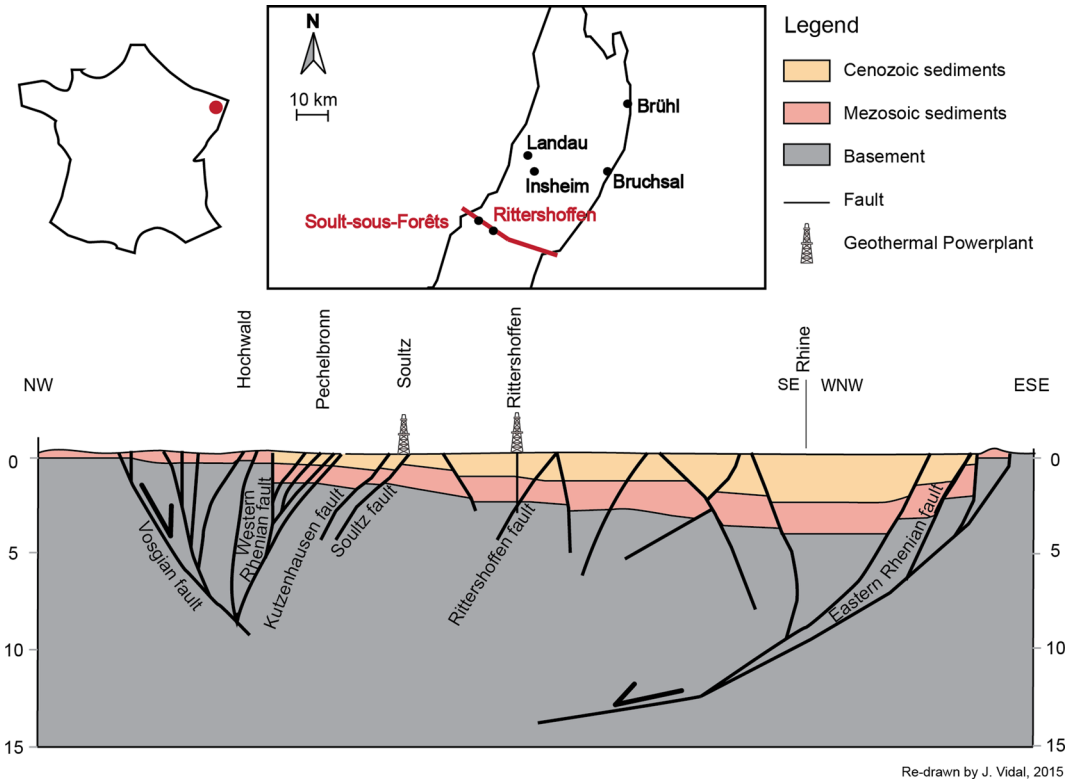

Figure 1. Location of the Rittershoffen geothermal site and geological cross-section through the Upper Rhine Graben at the latitude of Rittershoffen. The cross-section was modified after Kappelmeyer *et al.* (1992) and the interpretation below 4 km depth is done by analogy to the cross-section of Brun *et al.* (1992) and is highly speculative. An interpretative trajectory of GRT-1 crosses the Rittershoffen fault.

one newly permeable zone, and enhanced one originally permeable zone.

THE RITTERSHOFFEN SITE

Geological setting

The Rittershoffen site is located in the URG, which is a Cenozoic rift structure belonging to the European Cenozoic Rift System (Ziegler 1992). The first geothermal well drilled the site is located at 7.939°E and 48.897°N above the so-called Rittershoffen fault. This fault is located approximately 15 km east of the Western Rhenian border fault and is oriented N45°E (Fig. 1). This project takes advantages of the lessons learned from the Soultz geothermal pilot project located less than 10 km to the north-west of Rittershoffen. For example, mud-logging and well-logging data in the sedimentary cover of the geothermal boreholes at Soultz-sous-Forêts indicated the presence of permeable fractures in the Muschelkalk and Buntsandstein's formations (Vidal *et al.* 2015) and in the basement (Genter *et al.* 2000; Evans *et al.* 2005a; Dezayes *et al.* 2010). The initial target of the Soultz geothermal pilot project was the fracture network in the deep granitic basement, but it was observed that the fracture network at the sediment-basement interface is more permeable. Exploration geothermal well GRT-1 penetrates geologic units similar to those encountered in the Soultz wells. Fractures of similar permeability were expected, and the target of well GRT-1 was a geothermal reservoir at the sediment-basement interface. Its open-hole section penetrates approximately 300 m of sediments and 350 m of granitic basement. The lower portion of the sedimentary cover is composed of the Buntsandstein and Permian's sandstones. The Palaeozoic granitic basement, encountered at a depth of approximately 2210 m, is divided into three units: 50 m of reddish granite, 100 m of hydrothermally altered granite and 200 m of fine-grained fresh granite. The Paleozoic granitic basement was affected by pre-Cenozoic tectonics, particularly the Hercynian orogeny. The top of the granitic basement was affected by post-orogenic exhumation and subsequent palaeoweathering causing sub-horizontal jointing and a general reddish colour of the granite matrix respectively. Uplift of the top basement involved an uploading of the rock mass and the formation of horizontal fractures called jointing. Despite the high fracture density, the reddish granitic section of the top basement is not an aquifer as it was demonstrated by a packer test in GPK-1 between 1375 and 1395-m depth. Residual permeability in the granite is intimately linked to Hydrothermally Altered Fractured Zones showing a cluster organization deeper in the granitic basement (Genter *et al.* 2000). Well GRT-1 was drilled at the south-east of the horst to intersect the so-called Rittershoffen fault at the top of the basement (Fig. 1). Based on a seismic reflection section, this fault strikes N–S, dips westwards and displays a vertical offset of approximately 200 m. These Rhenish-oriented fractures are Hercynian structures (Illies 1972, 1975) that were reactivated during the Oligocene opening of the URG (Villemin & Bergerat 1987).

Drilling and stimulation operations

Well GRT-1 was drilled from September to December 2012 (Fig. 2). Subsequent production tests indicated that a major permeable structure controlling 2/3 of the flow was intersected at the 2368-m depth. However, the initial injectivity of the well was low and insufficient for industrial exploitation. The natural permeability of the

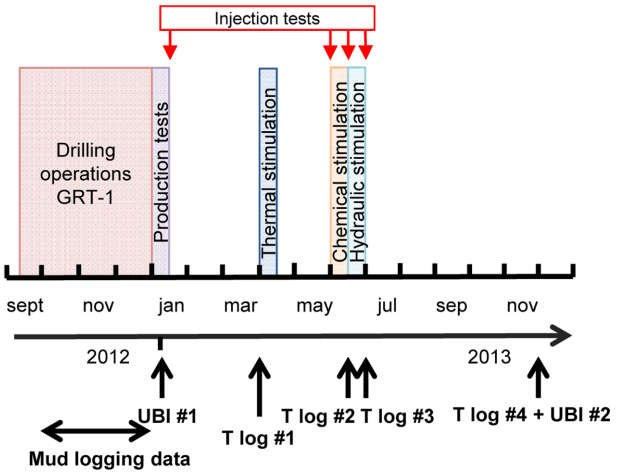

Figure 2. Chronology of stimulation and well-logging operations in well GRT-1.

Table 1. Increase in injectivity index of well GRT-1 following the TCH stimulation and expected radius of influence of each operation. Radius of influence of stimulations are from Schulte *et al.* (2010).

Stimulation	Increase in injectivity index after stimulation	Radius of influence
Thermal	x2	Near-well field
Chemical	x1.70	Near-well field
Hydraulic	x1.50	Far-well field

sedimentary and granitic parts was very low due to the poor hydraulic connectivity between the well and the fracture network and needed to be increased via TCH stimulation. Stimulation of well GRT-1 consisted of three phases: thermal stimulation, chemical stimulation and hydraulic stimulation.

The thermal stimulation consisted of cold-water injection from the wellhead 4 months after the drilling. During a time span of more than 60 hr, 4200 m^3 of water at surface temperatures was injected into the hot reservoir to encourage thermal microcracking along the wellbore, thereby increasing connectivity with the reservoir. More precisely, this cold-water injection caused microcracking of the quartz grains in the silicate matrix and fracture fillings (Griffiths *et al.* 2015). Thermoelastic effects reducing the normal stress on fractures and thus promoting fracture opening could be also envisaged (Dempsey *et al.* 2014). THM modelling of stimulated permeable fracture zones after cold-water injection into the granite rock reservoir of Soultz-sous-Forêts suggested the creation of a halo of alteration of thermos-mechanical origin and microcracking of surrounding quartz veins (Hosni *et al.* 2003). Microcracking in secondary quartz is ubiquitous within fractures and the coalescence of microcracks would improve fracture permeability. Thermal stimulation is typically performed to enhance the near-well field permeability, which may have been reduced by drilling (cuttings and mud clogging feed zones), and thus this stimulation is generally performed immediately following the drilling (Schulte *et al.* 2010; Grant *et al.* 2013). This technique is not usually applied to EGS geothermal wells in the URG but has produced satisfactory results in high-temperature systems in volcanic environments (Tulinius *et al.* 2000; Axelsson *et al.* 2006). Following the thermal treatment of well GRT-1, an injection test is performed two months later (Fig. 2) and the injectivity index was increased twofold (Table 1). All permeability increases given in this paragraph are considered as permanent and calculated from injection tests performed when the well was at the thermal equilibrium. Hydraulic data and injectivity calculations are not detailed in this manuscript.

The chemical stimulation was performed two months after the thermal operation. The chemical stimulation consisted of injecting an acid fluid to dissolve materials around the wellbore such as cuttings from the drilling and hydrothermal minerals plugging the fracture zones. This technology, which was developed and used by the oil and gas industry for more than a century (Economides & Nolte 1989), has been adapted to deep geothermal wells during the previous 20 yr to enhance the fracture network, particularly in EGS projects (Rose *et al.* 2007; Nami *et al.* 2008; Portier *et al.* 2009). The chemical stimulation of well GRT-1 targeted minerals that plugged the fracture zones. The stimulated zones and targeted minerals were identified from the cuttings and the post-drilling well-logging data from well GRT-1. The stimulation was performed using the biodegradable chelating agent GLTA (glutanic acid N, N – diacetic acid) to dissolve carbonates (calcite, dolomite, ankerite) and sulphates (Recalde Lummer *et al.* 2014). This environmentally friendly fluid does not dissolve alumino-silicates (clay minerals, quartz), is effective up to 200 °C and penetrates more deeply into the rock mass than conventional stimulation fluids. To avoid losing a large volume of acid fluid into the major permeable structure in well GRT-1 at the 2368-m depth, a single packer connected to coiled tubing was installed at three depths to concentrate the fluid treatment in specific intervals. Three intervals were chemically stimulated: one in the unaltered deep granite, one in the hydrothermally altered fractured granite of the upper basement and one in the Buntsandstein sandstones (Fig. 3). First, to treat the deepest zone, a single packer was installed at the 2368-m depth, and 120 m^3 of the stimulation fluid was injected below. Then, to treat the intermediate zone, a single packer was installed at the 2340-m depth, and 43 m^3 was injected. During the injection through the coiled tubing, the pressure injection is controlled and considered as sustainable. Assuming the chemical fluid penetrates uniformly the rock mass and considering the volume of chemical fluid injected and the volume of the well at the stimulated zone, the height of the stimulated zone is estimated to 40 m above 2340-m depth. Finally, to treat the shallowest zone, a single packer was installed at the 2010-m depth, and 87 m^3 of stimulation fluid was injected up to the casing shoe at the 1924.5-m depth. After the chemical treatments, the injectivity index increased by a factor of 1.70 (Table 1).

Two days afterward, the hydraulic stimulation was applied to the open section of the well to physically reactivate existing fractures. Hydraulic stimulation typically consists of injection of a large amount of water at a high flow rate to increase the pore pressure within the rock mass, which reduces the effective stress and promotes shearing of existing weak fractures in friction mode or the creation of new fractures either in shear mode if a significant natural differential stress (i.e. σ_1–σ_3) exists or in mode I tension when the in-situ shear stresses are very small and the fluid pressure is very high (Pine & Batchelor 1984; Cornet 1987; Schmittbuhl *et al.* 2014). It was demonstrated that this technology is efficient in both sedimentary and crystalline reservoirs (Baumgärtner *et al.* 2005; Huenges *et al.* 2007; Häring *et al.* 2008; Schindler *et al.* 2010) but might generate significant induced seismicity (Majer *et al.* 2007; Cuenot *et al.* 2008; Bromley & Majer 2012; Mukuhira *et al.* 2013). At Soultz-sous-Forêts, high-precision mapping of the induced seismicity delineated the great extent of hydrothermally altered zones where permeability enhancement primarily occurred (Evans *et al.* 2005a). Most of the flow entered the cores of the major permeable fault zones, whereas clusters of new permeable fractures indicate

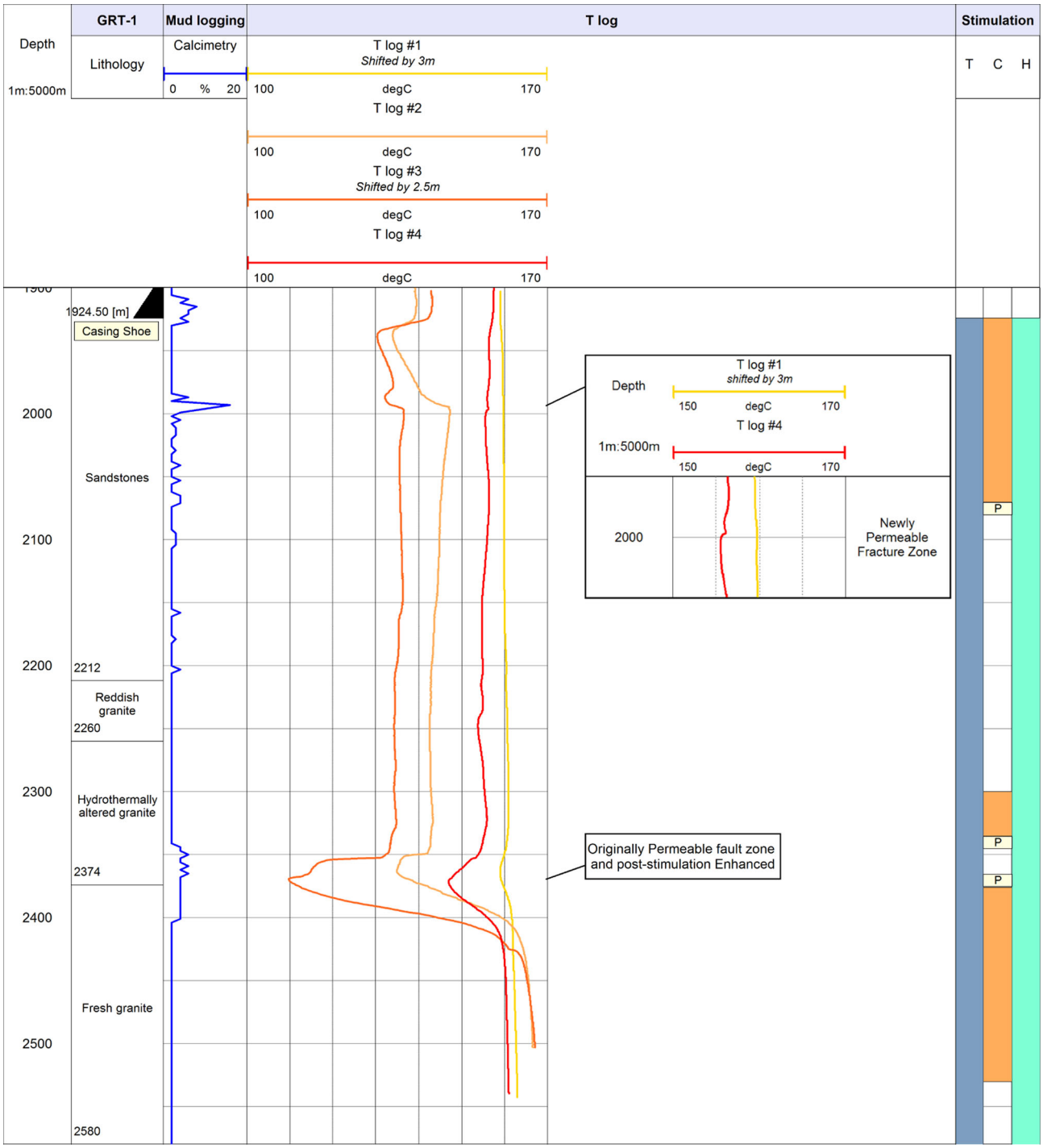

Figure 3. Composite log of well GRT-1. Calcimetry was measured by the mud-logging company. *T* logging operations were performed before the stimulations (*T* log #1), during the hydrochemical stimulation (*T* logs #2 and #3) and following the stimulations (*T* log #4). Stimulation zones are indicated.

the zone of damage to the fault (Evans *et al.* 2005b). A comparison of borehole image logs before and after the hydraulic stimulation indicated that all the permeable fractures had undergone mechanical damage and that major flowing fractures displayed dislocations of millimetres to centimetres. Some of these deformations at the centimetre scale in the deep reservoir of Soultz are slow deformations associated with aseismic events (Cornet *et al.* 1997; Schmittbuhl *et al.* 2014). Thus, induced microseismicity is not always a good indication of the efficiency of the hydraulic stimulation and permeability enhancement.

During the hydraulic operation in well GRT-1, a moderate volume (3250 m^3) of water was injected from the wellhead by increasing the flow rate in steps from 10 L s^{-1} to 80 L s^{-1} and then stepping down the flow rate to 10 L s^{-1}. No proppant or packer was used during the hydraulic stimulation, and the injectivity index was improved by a factor of 1.50. After the TCH treatments, the injectivity of well GRT-1 increased fivefold. Only a few significant microseismic events were recorded during the thermal stimulation, approximately a couple of hundred events were detected by the automatic detection system during the hydraulic stimulations based on data from

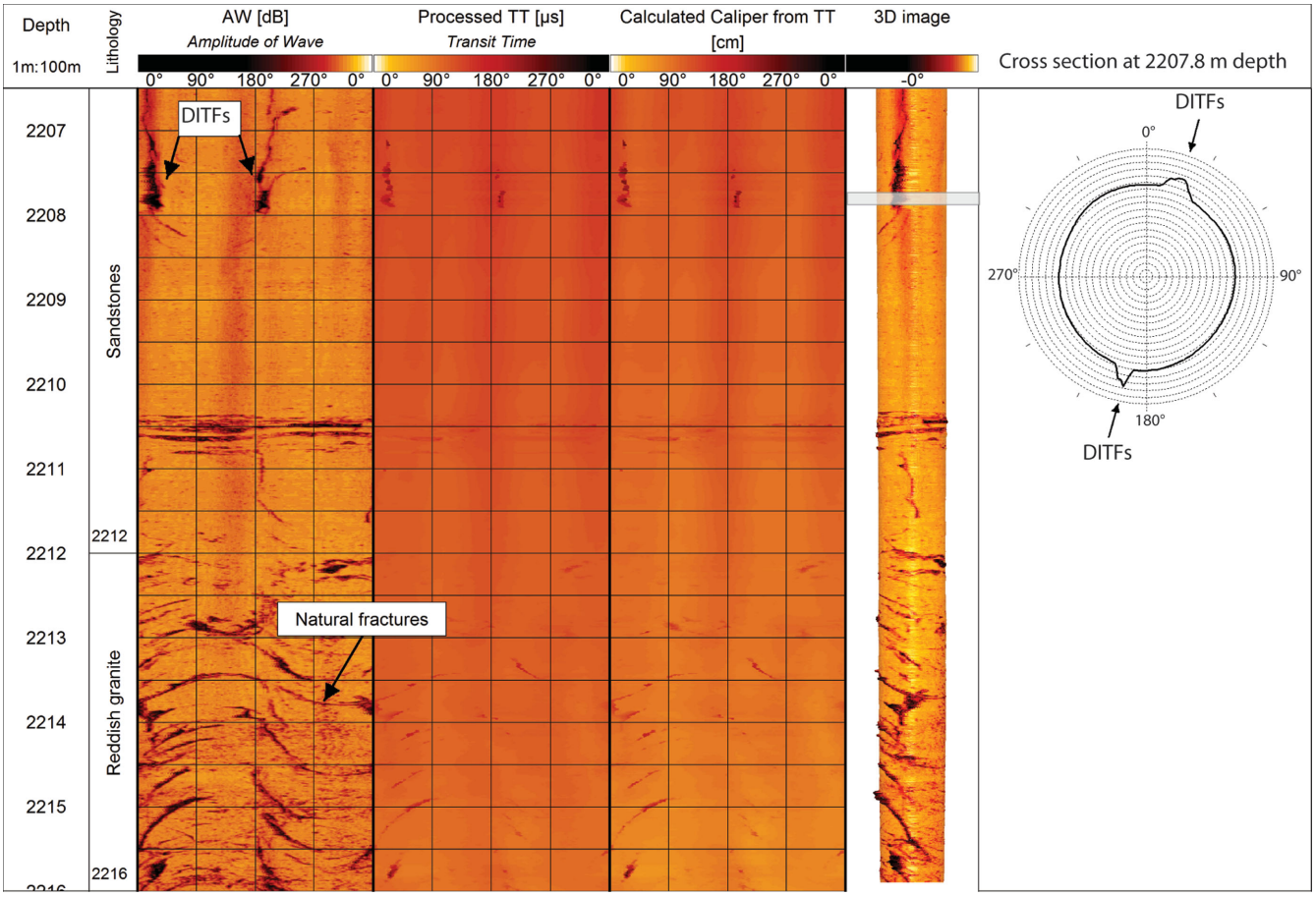

Figure 4. Example of acoustic image logs at the sediment-basement interface in well GRT-1. An image of the diameter (cm) was developed from the processed transit time data (µs), and a 3-D image of the well was constructed. The colour scale applies to the amplitude data (dB). An averaged cross-section was drawn through the 2207.77–2207.83-m depth interval (grey frame in the 3-D image of the well). On the cross-section, the concentric patterns are spaced 1 cm apart, and the thick line denotes the wellbore.

the real-time seismic monitoring network deployed during the stimulation, and none occurred during the chemical simulation. Due to the low wellhead pressure during the stimulation operations, no events were felt by nearby residents (Maurer *et al.* 2015).

Well logging and mud logging

During all drilling operations, mud-logging data were recorded. Cuttings were collected from the drilling mud every 3 or 4 m of advancement, and their analysis provided a lithostratigraphic survey of the well. It also indicated where the well intersected major fractures based on the presence of secondary quartz and hydrothermal minerals and higher calcite content (Fig. 3). Investigation of the rock cuttings was an efficient method for identifying hydrothermally altered zones in the granite (Dezayes *et al.* 2014; Meller *et al.* 2014). To evaluate the geometry of these fractures, an acoustic image log was acquired following the drilling operations in December 2012 (Fig. 2). The present study is based on these acoustic image logs, which were produced by Schlumberger and are referred to as Ultrasonic Borehole Images (UBIs). This logging was performed using a transducer that emits an ultrasonic pulse towards the borehole wall and records the first echo (Zemaneck *et al.* 1970). The amplitude and transit time of the reflected signal generate two unwrapped borehole images (Fig. 4). The amplitude data correspond to the energy of the reflected signal, that is, the reflectivity of the borehole wall. The transit time of the pulse from the transducer to the wall and its return is related to the geometry of the borehole and the acoustic velocity in the wellbore mud. The transducer is rotated as it advances, which allows it to create a complete map of the wall as the tool travels a spiral trajectory. An orientation tool consisting of a three-axis inclinometer and a three-axis magnetometer is added to the probe to orient the images with respect to magnetic north (Serra 2008). It is thereby possible to map the fracture orientations along the well (Davatzes & Hickman 2005). Natural fractures intersecting the well appear as continuous sinusoidal traces. The amplitude and phase of these traces provide quantitative estimates of their orientations (Fig. 4). If this sine wave is also visible in the transit time image, then the fracture is interpreted as an open structure at least at the borehole scale. If not, then the fracture is assumed to be completely or partly filled with secondary deposits. Acoustic image logs are also commonly used to identify borehole breakouts and drilling-induced tensile fractures (DITFs), which are important indicators of the stress state around the borehole (Valley & Evans 2007; Tingay *et al.* 2008). DITFs are narrow, sharply defined features (Fig. 4) that are produced when the tensile stress around the wellbore exceeds the tensile strength of the formation (Brudy & Zoback 1999). They are created along the azimuth of the maximum horizontal stress, that is, perpendicular to the breakout direction. They also appear in pairs 180° apart and are typically vertical in a near-vertical well (Fig. 4). Characteristics of DITFs are sensitive to the mud weight

and to thermal stresses induced by the cooling of the borehole wall during circulation of drilling fluids. The lithology can also be identified in acoustic image logs. For example, in Fig. 4, the Permian sandstones are affected by DITFs, and the contact with the underlying basement, which is cut by natural fractures with low dips, is well defined. The sediment-basement interface is difficult to identify based on mud logging primarily because the cuttings from both formations are very similar: the cuttings from reddish sandstone containing clasts of altered granite are difficult to distinguish from cuttings from reddish altered granite. The pre-stimulation acoustic image logs of well GRT-1 were acquired at a vertical resolution of 1 cm and an azimuthal resolution of 2°. The inclinometer provided vertical deviations accurate to ±2°, and azimuthal measurements accurate to ±0.5° at the latitude of Paris.

The temperature (*T*) logs obtained during the stimulation were a cost-effective way of assessing the stimulation success. Specifically, local variations in the *T* logs typically reflect remnant cooling of permeable fractures following the stimulation injections. Four *T* logging operations were performed in well GRT-1 in 2013 (Figs 2 and 3). *T* log #1 was the pre-stimulation *T* log and was obtained four months after the drilling but before the thermal stimulation. The well was not disturbed during this period following the acidification in January. The sampling resolution of *T* log #1 was 0.10 m. The second log, *T* log #2, was the post-C-stimulation *T* log, which was obtained after the chemical stimulation and thus was highly affected by the fluid injection. The third log, *T* log #3, was the post-H-stimulation *T* log and was obtained after the hydraulic stimulation, that is, two days following the chemical treatment. The sampling resolution of *T* logs #2 and #3 was 0.20 m. The last log, *T* log #4, was the post-stimulation *T* log and was obtained five months later under thermal equilibrium conditions. The sampling resolution of *T* log #4 was 0.15 m. In December 2013, a second acoustic image log of well GRT-1 was obtained (Fig. 2) with a vertical resolution of 1 cm and an azimuthal resolution of 2°. Acoustic imaging surveys are a very useful method for assessing the fracture network enhancement based on a comparison of pre- and post-stimulation data (Cornet *et al.* 1997). This technique is not commonly used in EGS project. The goal of the present study was to assess the information by comparing the pre- and post-stimulation data sets and to answer questions such as the following: What modifications may be discerned by comparing two acoustic image logs? What is the resolution of the comparison? Does the comparison between pre- and post-stimulation acoustic image logs contribute significantly to the assessment of the stimulation compared to *T* logs?

METHODOLOGY

Data processing of acoustic image logs

The acoustic image logs were processed using the software program WellCAD (ALT). First, the amplitude (AW) data and transit times (TT) in the image logs recorded in 2012 were reoriented with respect to magnetic north based on the azimuths acquired by the orientation tool. In 2013, unfortunately, the orientation tool was missing during the acquisition. Thus, the 2013 images were reoriented manually by visually superimposing 2013 images on the 2012 images. The manually reoriented images were rotated clockwise by an angle that varied with depth based on the rotation of the acoustic tool during the up-hole acquisition. The variation in the offset angle is important, and uniform rotation by a fixed angle in a long vertical section is not possible. This manual correction method is adequate for a localized zone, and the choice of the offset angle is well defined where natural fractures exist and is approximate where few patterns are present in the images. Depth mismatches were observed locally; these were due to cable expansion related to the temperature increase along the well or to a decrease in the acquisition speed related to abnormal borehole wall roughness associated with cavities. Depth corrections were applied to the image logs and data set of 2013 when depth differences exceeded 6 cm.

Table 2. Error bars (calculated from standard deviation) for the diameters measured in 2012 and 2013.

Tool calibration	Diameter (cm)	Error Bar (cm)
Casing	22.05	
2012 measurement	22.17	0.011
2013 measurement	21.95	0.017
Massive zone in sandstones		
2012 measurement	21.01	0.095
2013 measurement	20.8	0.084

Once the transit time images were reoriented, they were corrected for decentralization effects that are negligible in GRT-1 with the average eccentering value of 0.38 cm in 2012 and 0.56 cm in 2013. They were also smoothed to remove spikes that are typically related to erroneous data recordings. The smoothing method consisted of a cut-off based on 3 × 3 window analysis. One cut-off high level (75 per cent) and one cut-off low level (25 per cent) were applied. If the data value exceeded the cut-off, it was replaced with the cut-off value.

The processed transit time data were used to develop a 3-D image of the borehole based on the slowness of the acoustic wave in the mud measured using the acoustic tool in the well (Fig. 4). In 2012, the acoustic tool used for acquisition was appropriate to image well-diameter in the range of 20–22.6 cm. In 2013, the acoustic tool used for acquisition was appropriate to image well-diameter between 18.6 and 20 cm. Measurements outside the pre-defined ranges are possible, but errors are expected to be large. For this study, we performed a posteriori calibration to estimate error bars of the acoustic borehole diameter measurements. The standard deviation was estimated from the transit time in 2012 and 2013 for different average diameter. We used the casing of well GRT-1 as a fixed reference that did not vary with depth or time. Its internal diameter given by the manufacturer is 22.05 cm. We then measured this casing diameter using the acoustic tool both in 2012 and 2013. The average diameter estimated from the transit time in 2012 was 22.17 cm ±0.011, which indicates a systematic error of +1.2 mm with respect to the reference value (Table 2). Accordingly, all the calculated diameter data obtained in 2012 were then reduced by 1.2 mm. The average diameter estimated from the transit time in 2013 was 21.95 cm ± 0.017, and the acoustic tool measurements obtained in 2013 were reduced accordingly by 1 mm. The source of error between measurements in 2012, 2013 and the given value of the internal diameter is assumed to be governed by the error on the internal diameter given by the constructor. When the acoustic tools encountered cavities in the borehole wall, the diameters exceeded the acquisition range, and null data were recorded. In these instances, the transit time data appear as saturated zones, that is, white spots, in the images.

A 3-D image of the well was constructed by mapping the acoustic image onto the geometry provided by the transit times and using the amplitude data to create the colour palette in the 3-D image (Fig. 4). From this 3-D image, cross-sections of the well were prepared. Another technique was developed to assess error bars of the diameter

data in the sandstones. A massive zone (one not cut by fractures) was identified between depths of 2208 and 2210.5 m (Fig. 4). The rms of this zone was ±0.095 cm in 2012 and ±0.084 cm in 2013 (Table 2). Thus, for each cross-section, the thickness of the line in Fig. 4, which is on the order of 1 mm, incorporates the error bars of the acoustic diameter.

Based on the acoustic diameter data set, a transverse cross-section was developed for each centimetre of depth. Nevertheless, because vertical mismatches between the 2012 and 2013 images were as much as approximately 6 cm, the cross-sections developed in this study represent 6-cm-thick slices to ensure that individual geologic structures could be identified and matched in the images of both years. Thus, a cross-section at a given depth is a representation of the average of slices on an interval ranging from 3 cm above to 3 cm below the given depth. The same types of corrections were applied to the amplitude data. Based on these corrected acoustic image logs and associated cross-sections, modifications of the fracture zones and mechanical movements of the wellbore were interpreted. Accuracies of the fracture attitudes are important for the comparison of the 2012 and 2013 images. In this study, the primary source of error in the fracture dip direction and dip angle arose from the ability of the interpreter to pick dipping planes consistently. To quantify the accuracy of measurements from the acoustic image log in the open-hole section of well GRT-1, a series of tests were performed. These tests involved three acoustic image interpreters who hand-measured strikes and dips independently in the hydrothermally altered granite section. The reproducibility error was ±3.85° for the strikes and ±1.04° for the dips. The overall error considering the inclinometer accuracy and the reproducibility error may be regarded as very low.

The colour scale of the amplitude and transit time data were adjusted visually. The amplitude and transit time values are comparable in the internal diameter of the casing and assumed as a fixed reference in 2012 and 2013. Thus, this reference zone was used to determine the colour scale in order to compare the rest of the open-hole section with uniform colour scales.

Data processing of mud-logging data and *T* logs

To maintain a single depth reference for all the well data in the study, the gamma ray log obtained during the pre-stimulation acoustic logging was used as the baseline. Detailed mud-logging data (rate of penetration (ROP), gas content, drilling parameters) were not processed in this study. All *T* logging operations were performed downhole at a constant velocity of tool advancement. They were performed, however, by different loggers. *T* log #1 was shifted downwards by 3 m to obtain a match with the gamma ray log (Fig. 3). *T* logs #2 and #3 were obtained without the use of the gamma ray probe, and thus they were adjusted based on the position of a negative anomaly between depths of 1924.5 and 1994.5 m in *T* log #2 and 1921.5 and 1995 m in *T* log #3. This negative anomaly is well known from geothermal wells in Soultz and Landau and corresponds to fractures below the casing shoe that are zones initially affected by the cold-water injections (Schindler *et al.* 2010). The image logs show the casing shoe at the 1924.5-m depth. *T* log #2 was not shifted, and *T* log #3 was shifted downwards by 3 m to ensure a match between the distances from the top of the anomaly and the position of the casing shoe. The temperature probe used to acquire *T* logs #2 and #3 experienced technical problems during the acquisition. The bottom hole temperature in *T* log #1, considered to be the temperature under conditions of thermal equilibrium, was 163 °C. The bottom hole temperatures in *T* logs #2 and #3 exceeded 166 °C, although the well was supposedly cooled by the chemical and hydraulic treatments. These technical problems during the acquisition may have affected the data to an unknown extent. However, although the temperature data in *T* logs #2 and #3 may be inaccurate in absolute terms, the major anomalies were taken into account in relative terms. *T* log #4 was not shifted.

Evaluation of permeability enhancement

To evaluate the impact of the TCH stimulation in well GRT-1, the pre- and post-acoustic image logs were correlated and compared with the *T* logs.

The mud-logging survey indicates that the natural fractures are filled with carbonates and sulphates. Any modifications of this fracturing in the post-stimulation UBI amplitude data indicate that mineral dissolution occurred with the chemical treatments. Chemical alteration is localized around fracture zones and is observed in the UBI amplitude data and in the transverse cross-sections. A re-opening of the natural fractures in the post-stimulation cross-section may also be associated with hydromechanical impacts due to the hydraulic stimulation. Re-activation of an existing fracture could be interpreted in several ways. One is dip slip along the fracture (Fig. 5), in which case this displacement needs to be evaluated. The mean borehole cross-section is assumed to be circular before slip has occurred, and the centre of this circular cross-section is the centre of the well. If displacement has occurred, then the mean

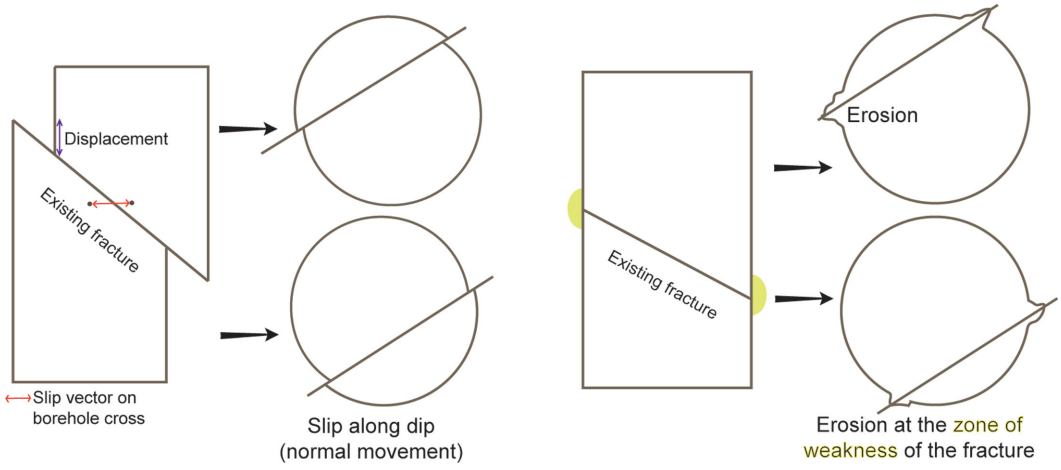

Figure 5. Dip slip along an existing fracture and erosion at the intersection between the fracture and the borehole wall.

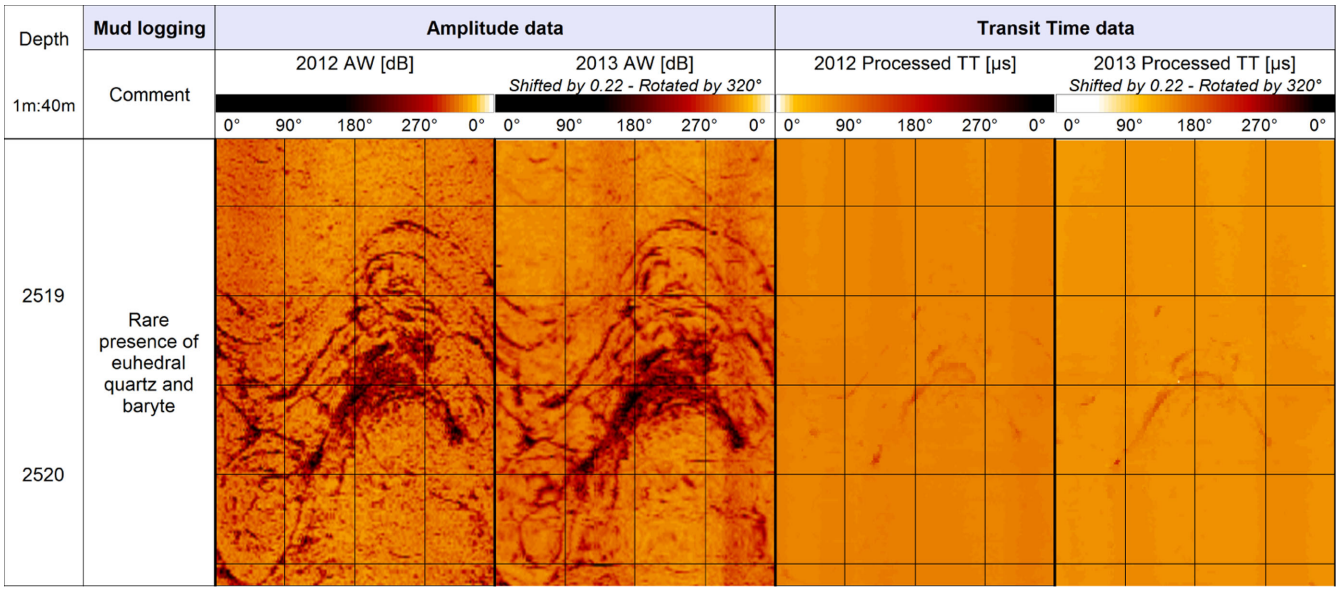

Figure 6. Comparison of acoustic image logs before and after the TCH stimulations showing a post-stimulation unmodified zone in the fresh granite. Amplitude data are expressed in dB, and transit time data in µs.

borehole cross-section does not match the initial one, and the centre of the post-stimulation well will appear to have shifted. The relative displacement along the fracture can be defined by a vector between two points on either side of the fracture. The displacement is the projection of this vector onto the cross-section through the well. Another possible interpretation is erosion of the wall at the intersection with the fracture plane because the fracture is a zone of weakness (Fig. 5).

Because the acoustic image logs represent only conditions before and after all the TCH stimulations, the *T* logs yield additional information about the permeability enhancement along natural fractures between each stimulation operation. Negative anomalies on the *T* logs are the thermal signature of permeable fractures that were cooled by the drilling and massive hydraulic injections. Negative anomalies on the *T* logs indicate circulation of cold water through permeable fracture zones. To quantify the permeability enhancement if a negative anomaly, that is, colder after an injection, appears, parameters used during injection have to be taken in account such as the temperature of the injected fluid, the flow rates, the duration of the injections, and the pressure of the injection. . . Positive anomalies on the *T* logs indicate circulation of hot geothermal fluid through a permeable fracture zone. Moreover, *T* logs yield information about major fracture zones that were not imaged by the acoustic tool, for example, in instances of saturation.

A certain amount of saturation of the acoustic tools may also appear where the borehole is affected by significant breakouts and cavities. The appearance and deepening of a breakout on a post-stimulation image log are not necessarily associated with stimulation operations but may be a consequence of stress relaxation around the wellbore.

When evaluating the impact of the TCH stimulation on well GRT-1, the logs have been analysed for the following three patterns:

(1) no modification is visible in comparisons of the pre- and post-stimulation acoustic image logs;

(2) modifications are visible in comparisons of the pre- and post-stimulation acoustic image logs, but there is no corresponding temperature anomaly, which indicates the presence of an impermeable fracture zone;

(3) modifications are visible in comparisons of the acoustic image logs, and there are corresponding temperature anomalies. If the temperature anomaly is visible on the pre-stimulation *T* log and is cooler after the stimulation, then the fracture zone is classified as originally permeable and post-stimulation enhanced (OPE). If the temperature anomaly appears only on the post-stimulation *T* log, then the fracture zone is classified as newly permeable (NP).

RESULTS

All results established on the basis of well-logging and mud-logging data are given in Measured Depth.

Unmodified fracture zones

Unmodified zones were very rare based on the comparison of the pre- and post-stimulation data sets. The fresh granite below the major fault zone at the 2368-m depth was thermally, chemically and hydraulically stimulated. Fracture zones at substantial depths in the open-hole section were less affected by the thermal and hydraulic stimulations, which were performed either from the wellhead or from the packer at the 2368-m depth. The fracture zone in the 2518.8–2520.5-m depth interval consists of five primary natural fractures with a mean dip direction of N56°E and a mean dip of 83°E (Fig. 6). The post-stimulation amplitude and transit time images were shifted downwards by 0.22 m and rotated by 320° clockwise to match the oriented pre-stimulation image. The comparison between the pre- and post-stimulation amplitude images does not show evident modification around the fractures or in the granitic matrix. The same lack of modification was observed in the transit time images. In addition, the cross-sections show an unvarying well diameter in this interval.

Modified fracture zones with no permeability evolution

A few fracture zones in the uppermost fresh granite were affected by the TCH stimulation, for example the zone in the 2396–2400-m

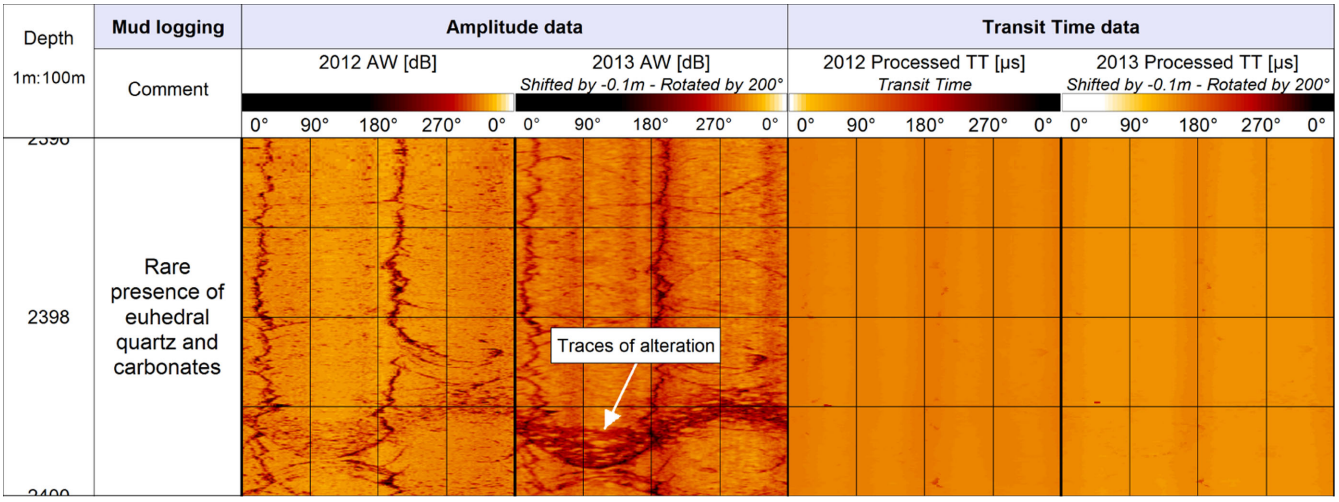

Figure 7. Comparison of acoustic image logs before and after the TCH stimulations showing a post-stimulation modified fracture with no permeability indication in the fresh granite. Amplitude data are expressed in dB, and transit time data in µs.

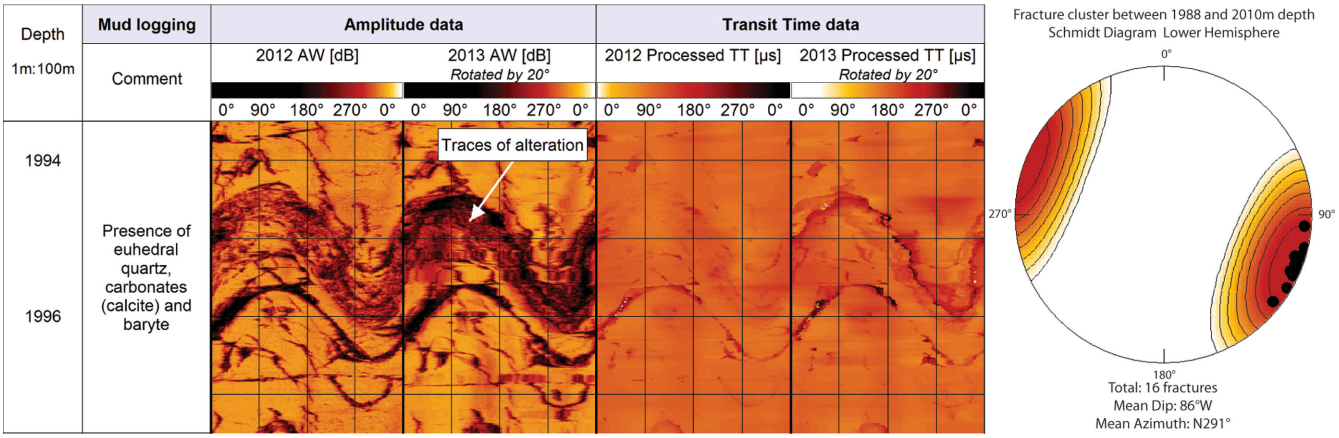

Figure 8. Comparison of acoustic image logs before and after the TCH stimulations in a newly permeable fracture zone in sandstones. The Schmidt diagram (lower hemisphere) shows the mean dip direction orientation (N21°E) and the mean dip (86°W) of the fracture cluster in the 1988–2010-m depth interval.

depth interval. This zone is dominated by DITFs striking N10°E and N190°E with one natural fracture at the 2399.3-m depth that strikes N24°E and dips 80°E (Fig. 7). The post-stimulation images were manually shifted upwards by 0.1 m and rotated by 200°E to match the oriented pre-stimulation image. In the pre-stimulation amplitude image, the fracture at the 2398.5-m depth is barely visible. The percentage of calcite is very low in this section, and the mud-logging survey indicates the presence of rare quartz and carbonates in the cuttings. In the post-stimulation amplitude image, the shape of the fracture is better defined, and traces of alteration are visible around the fracture. DITFs observed in the pre-stimulation amplitude data are more pronounced and wider in the post-stimulation amplitude data. Following the hydraulic injection, the DIFTs are wider. They may act as hydraulic connections between isolated fractures, but they are not associated with any perturbations in the thermal logs, which suggests that their involvement in the permeability enhancement is negligible. The natural fractures and DITFs are not visible in the transit time data, and no diameter anomaly is observed, and thus they are interpreted as superficial structures with no lateral penetration into the rock mass. This observation is valid below the top of the fresh granitic section, where there are tiny natural fractures more visible in the amplitude data that are increasingly less visible with depth.

Modified fracture zones with permeability evolution

Newly permeable fracture zone in sandstones

The section of sandstone under the casing shoe was thermally, chemically and hydraulically stimulated. The pre-stimulation acoustic image log in the 1988–2010-m depth interval presents a cluster of 16 fractures with a mean strike of N21°E and a mean dip of 86°W (Schmidt diagram in Fig. 8). The calcimetry shows peaks of 6 per cent calcite at the 1988-m depth, 16 per cent at the 1993-m depth and 10 per cent at the 1996-m depth (Fig. 3). This high calcite content in this zone is related to the fracture filling. Carbonates, barite and euhedral quartz were also observed in cuttings from this zone. The core of the cluster in the 1994–1997-m depth interval is shown in Fig. 8. Manual orientation of the post-simulation image of this zone to match the oriented pre-stimulation image was complex because the vertical and azimuthal shifts are not consistent. A schematic diagram of the zone is shown in Fig. 9. Point A is located at 1994.19 m at N208°E on the pre-stimulation image, and point A′ is located at the 1994.23-m depth at N186°E. Point C is located at the 1996.41-m depth at N90°E, and point C′ is located at the 1996.46-m depth at N104°E. The vertical and azimuthal shifts differ between the top and the bottom of the zone. Point B (1995.61 m, N118°E) and B′ represent the intersection between the base of the stratigraphic layer

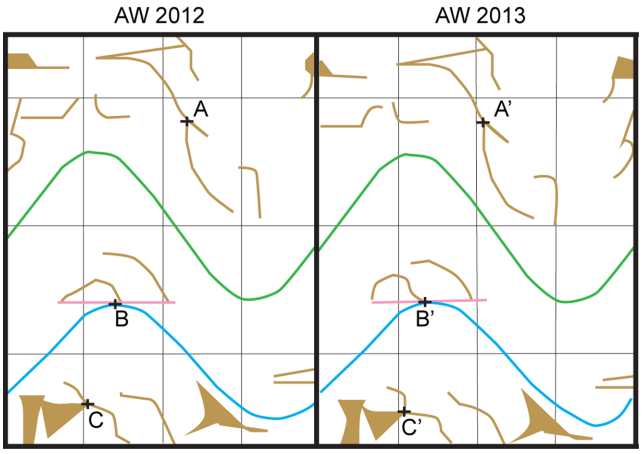

Figure 9. Schematic drawing of the fracture zone shown in Fig. 8.

(in pink) and the top of the fracture F2 (in blue). The position of the stratigraphic layer was confirmed based on the FMI data and serves as a good reference because it was not modified by the TCH stimulation. The post-stimulation image was rotated by 20° to achieve a match between points B′ and B, although this correction may not yield a match throughout the zone. No vertical shift was applied.

To compare the same geologic structures on the cross-sections in Fig. 10, the cross-sections are averages of 6-cm vertical intervals because the vertical shift never exceeds 6 cm. The core of the cluster contains two main fractures. One, designated F1, is located at the 1995.00-m depth, strikes N14°E and dips 85°W (Fig. 8). It is shown in green in Fig. 10. Another, designated F2, is located at the 1996-m depth, strikes N50°E, dips 83°W and has an aperture of 6 mm (Fig. 8). It is shown in blue in Fig. 10.

Fracture F1 displays lower amplitudes in the post-stimulation amplitude image than in the pre-stimulation image. A comparison of the pre- and post-stimulation cross-sections at the 1994.5-m depth indicates significant azimuthal enlargement (between 0.5 and 2.5 cm) from N40°E to N150°E (Fig. 10). The maximum enlargement of 2.5 cm is located between N80° and N150°, which corresponds to the trace of fracture F1 at this depth. Enlargements as wide as approximately 0.8 cm are also visible between N240°E and N330°E. Azimuthal shrinkages between 0.3 and 0.8 cm are also observed between N150°E and N220°E and between N330°E and N20°E. The post-stimulation cross-section at the 1995.50-m depth shows the bottom of fracture F1. Shrinkage between N300°E and N350°E corresponds to the intersection of the fracture trace with the well. Enlargements as wide as 3.5 cm at N250°E, 2 cm at N355°E and 1 cm at N20°E are associated with reactivation of another fracture near fracture F1. As in the

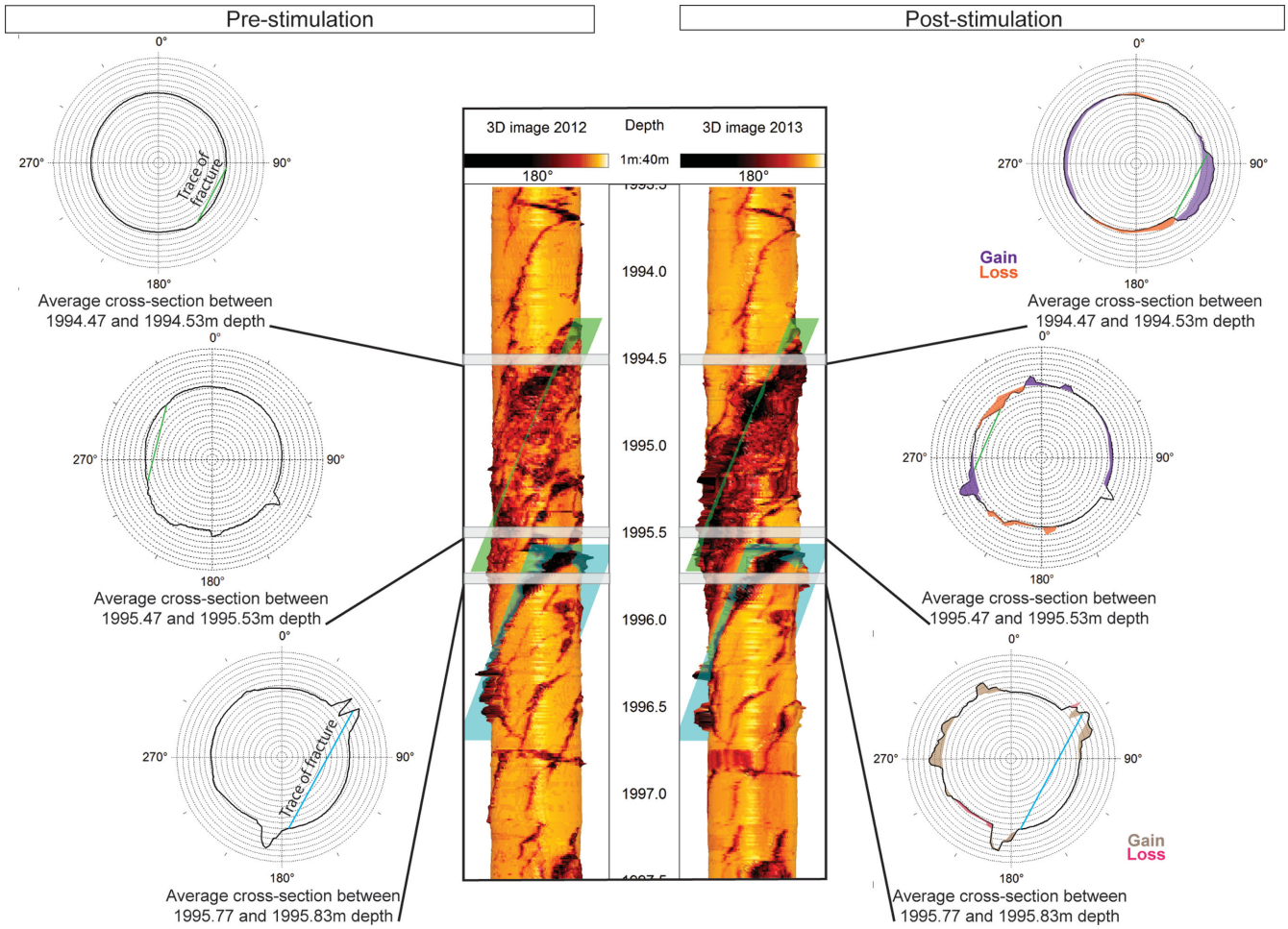

Figure 10. Average transverse cross-sections at the 1994.48- and 1994.52-m depths, at the 1995.48- and 1995.52-m depths and at the 1995.78- and 1995.82-m depths through stimulated fracture zones in the sandstones. The left and right cross-sections show conditions before and after the TCH stimulations, respectively. They are denoted by a grey frame in the 3-D image of the well. In the cross-section, the concentric patterns are spaced 1 cm apart, and the thick line denotes the wellbore.

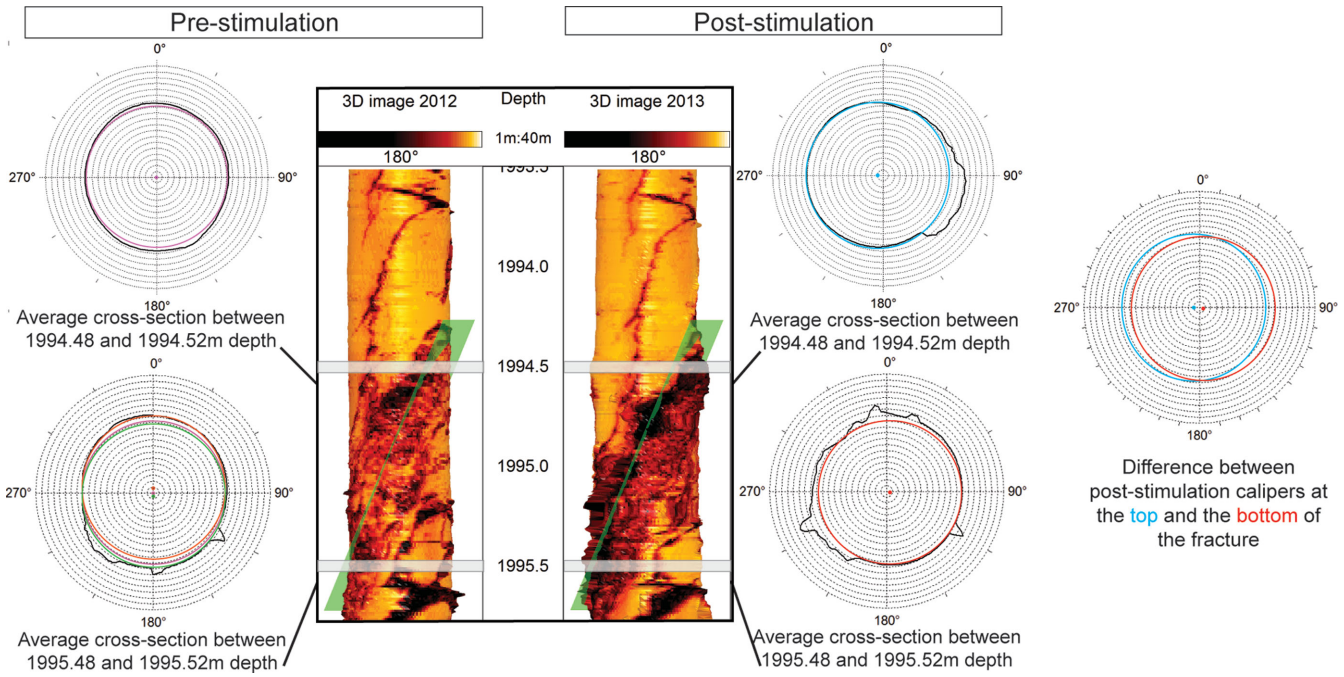

Figure 11. Determination of hydromechanical displacement along fracture F1. The pink circle denotes the theoretical 12-cm-diameter circle that fits in the pre-stimulation borehole at the 1994.5-m depth (top of F1). The orange and green circles denote theoretical 12-cm-diameter circles that fit the pre-stimulation borehole at the 1994.5-m depth (bottom of F1). The blue circle denotes the theoretical 12-cm-diameter circle that fits the post-stimulation cross-section at the 1994.5-m depth (top of F1), and the red circle denotes the theoretical 12-cm-diameter circle that fits the post-stimulation cross-section at the 1995.5-m depth (bottom of F1).

cross-section at the 1994.5-m depth, small shrinkages as wide as 1 cm are observed between N190°E and N220°E, and enlargements as wide as 0.5 cm are observed between N60°E and N110°E.

To interpret the observed morphology change of the borehole, we followed the procedure of Cornet *et al.* (1997). In the pre-stimulation cross-sections at depths of 1994.5 m (top of F1) and 1995.5 m (bottom of F1), circles with similar radii (12 cm) at both depths were searched for one that best fit both borehole traces at each depth (pink circle in Fig. 11). At the 1995.5-m depth, the orange and the green circles with similar radii also fit the cross-section. The uncertainty in the circle's centre position is 2 cm. On the post-stimulation cross-sections at the 1994.5-m depth, a blue circle with a radius of 12 cm fits the zone not affected by fractures between N180°E and N0°E. At the 1995.5-m depth, a red circle corresponding to the zone not affected by fractures between N90°E and N180°E was drawn on the post-stimulation cross-section. After the centres of the blue and red circles were plotted, a displacement vector of 2 cm between the centres was noted. Because this displacement is of the same magnitude as the uncertainty in the circle centre location, the displacement between the top and the bottom of fracture F1 is not considered significant.

Fracture F2 does not display distinct modifications in the post-stimulation amplitude image, whereas the top of the fracture is clearly visible in the post-stimulation transit time image (Fig. 8). A cross-section was drawn at the 1995.8-m depth based on the pre-stimulation diameter data, thereby allowing for observation of the trace and penetration of fracture F2 (Fig. 10). One branch of F2 that penetrates 4 cm into the rock mass is observed at N190°E, and a second branch that penetrates 3.5 cm into the rock mass consists of two peaks at N50°E and N60°E. The post-stimulation cross-section at that same depth shows enlargement and shrinkage of both peaks of 0.5 to 3 cm. Enlargements of 0.5 cm to 2.5 cm between N265°E and N300°E and N330°E and N355°E correspond to re-activation of the bottom of a fracture near fracture F1.

The post-stimulation *T* log indicates circulation of hot geothermal fluid through this fracture zone based on a positive *T* anomaly of +1 °C at the 1995.5-m depth that was not observed in the pre-stimulation *T* log (Fig. 3). Traces of alteration were observed in the post-stimulation amplitude data, fracture enlargements and shrinkages were observed in the diameter data, and a permeability enhancement was observed after comparing the pre- and post-stimulation *T* logs. Thus, this fracture zone is classified as a newly permeable fracture zone.

Originally permeable and post-stimulation enhanced fracture zone in granite

The pre-stimulation acoustic image log at the 2368-m depth shows a major structure at the base of the hydrothermally altered granitic section that strikes N175°E, dips 65°W and has an aperture of 24 cm (Fig. 12). This structure is interpreted as a branch of the Rittershoffen fault where it was crossed by the well. The hanging wall of this fault zone consists of hydrothermally altered granite, whereas the foot wall consists of fresh granite. The fault is originally permeable as indicated by mud losses of 8 to 10 m^3/h during the drilling (Fig. 12) and the negative *T* anomaly on the pre-stimulation log (Fig. 3). Abundant euhedral quartz was observed in the cuttings from this zone: this material is interpreted as a quartz vein within the fault zone based on findings from the Soultz-sous-Forêts boreholes (Genter *et al.* 2000). To enhance the permeability of the fault zone, it was thermally and hydraulically stimulated. The transit time data from this zone are not useable and are saturated in the pre- and post-stimulation images (Fig. 12) because the well diameter exceeded the range of the acoustic tools. The drill bit penetration rate

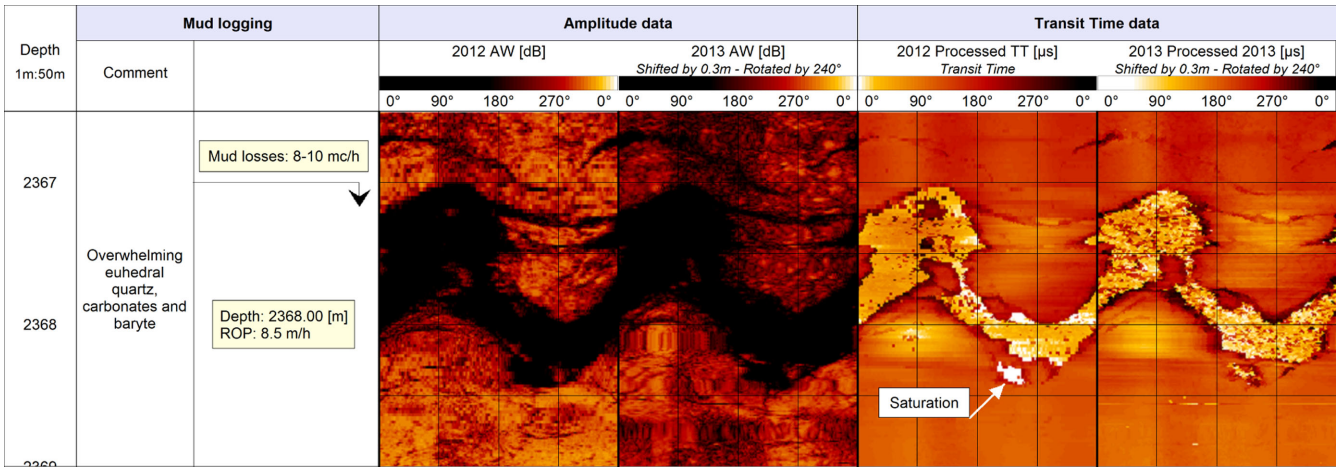

Figure 12. Comparison of acoustic image logs before and after the TCH stimulations showing an originally permeable and post-stimulation enhanced fault zone in the hydrothermally altered granite. Amplitude data are expressed in dB, and transit time data in µs.

in the 2368-m depth was double the mean rate in the granitic section, which indicates that the fault zone is borehole enlargement (Traineau *et al.* 1992). The post-stimulation acoustic image log was manually shifted downwards by 0.3 m and rotated by N240°E to match the oriented pre-stimulation image log (Fig. 12). Although quartz veins are not observed in the amplitude image, quartz veins in the fault probably also underwent thermal microcracking because the *T* logs suggest permeability enhancement following the water injections. A comparison of the *T* logs yields information about the permeability enhancement. The pre-stimulation *T* log shows a negative anomaly of −1 °C in the 2350–2375-m depth interval and a temperature of 158 °C at the 2365-m depth. Following the chemical injections, the *T* log shows a negative anomaly of −5 °C between the 2350- and 2370-m depths. Following the hydraulic injections, the *T* log shows a negative anomaly of −15 °C between the 2355- and 2365-m depths and a small peak of 109 °C at the 2370-m depth. In the post-stimulation *T* log, the negative anomaly spans the 2352–2395-m depth interval and shows a small peak of 147 °C at the 2372-m depth. This *T* anomaly corresponding to the fault zone is the largest anomaly in the *T* logs (Fig. 3). The increase of the temperature anomaly following the TCH stimulation can be interpreted as fluid circulation through the fault zone and could correspond to a permeability enhancement. Although no modifications are visible in a comparison of the acoustic image logs, the pre-stimulation acoustic image log, the mud-logging data and the comparison of the *T* logs indicate that this fault zone is classified as originally permeable and post-stimulation enhanced.

DISCUSSION

Insights from the pre-stimulation data set

The acoustic image log is one of the few well-logging tools that provides in-situ orientation of the fracture network and stress field. It is also useful in characterizing the stratigraphy of the sedimentary units and altered facies in the granite. The sediment-basement interface is well constrained based on the acoustic image of well GRT-1, which is of better resolution than the mud-logging data (Fig. 4). The hydrothermally altered zones in the granite are clearly shown in the acoustic image in terms of their thicknesses, orientations, apertures, and dips. The high reflectivity of quartz allows for identification of quartz veins. The pre-stimulation acoustic image log combined with the mud-logging data (e.g. the calcimetry) allows for characterizing the geometry of the major permeable fault zone crossing the well, identifying the potential zone for the TCH stimulation and designing the TCH stimulation. The pre-stimulation *T* log shows a nearly constant temperature profile with depth (Fig. 3) that is typical of convective systems in high-enthalpy geothermal fields (Arnórsson 1995; Guillou-Frottier & Jaupard 1995; Ikeuchi *et al.* 1998; Guillou-Frottier 2003; Magnenet *et al.* 2014; Ratouis & Zarrouk 2016). Our interpretation is that the geothermal fluid circulates vertically in the bulk rock through a dense, diffuse network of permeable fractures at the sediment-basement interface next to the major fault zone. The TCH stimulation of well GRT-1 was performed to enhance the permeability of this fracture network.

Insights from the post-stimulation data set

The comparison of the pre- and post-stimulation acoustic image logs reveals several modifications of the well following the TCH stimulation throughout the open-hole section except for the deepest part. These modifications can be classified as chemical and thermo-hydro-mechanical damage (Fig. 13). Note that the damage is not characterized as mechanical evolution of the material properties related to microfracture propagation but as a generic description of the impact of the stimulation on the formation. All natural fractures except a few in the deep part of the borehole that were not affected by injection display visible modification in the post-stimulation acoustic image, although this modification does not necessarily impact the permeability of the well.

The chemical alteration consists of local impacts around or within fracture zones and a halo of dissolution following their sinusoidal traces. In the sandstones, a high density of fractures in the 1988–2010-m depth interval without major displacement was observed. The entire sandstone formation in GRT-1 is 400-m thick which corresponds to the standard thickness of this formation in Northern Alsace (Ménillet *et al.* 2015). These fractures do not show natural permeability but do contain a high amount of calcite. The dissolution of carbonates and the opening of natural fractures F1 and F2 at the core of this cluster (Fig. 8) were observed in the amplitude data from the post-stimulation image logs. Specifically, the reflected amplitudes are lower in the post-stimulation amplitude data and cross-sections are enlarged in the post-stimulation data. In the cross-sections, fracture F1 in the sandstone displays enlargements at the

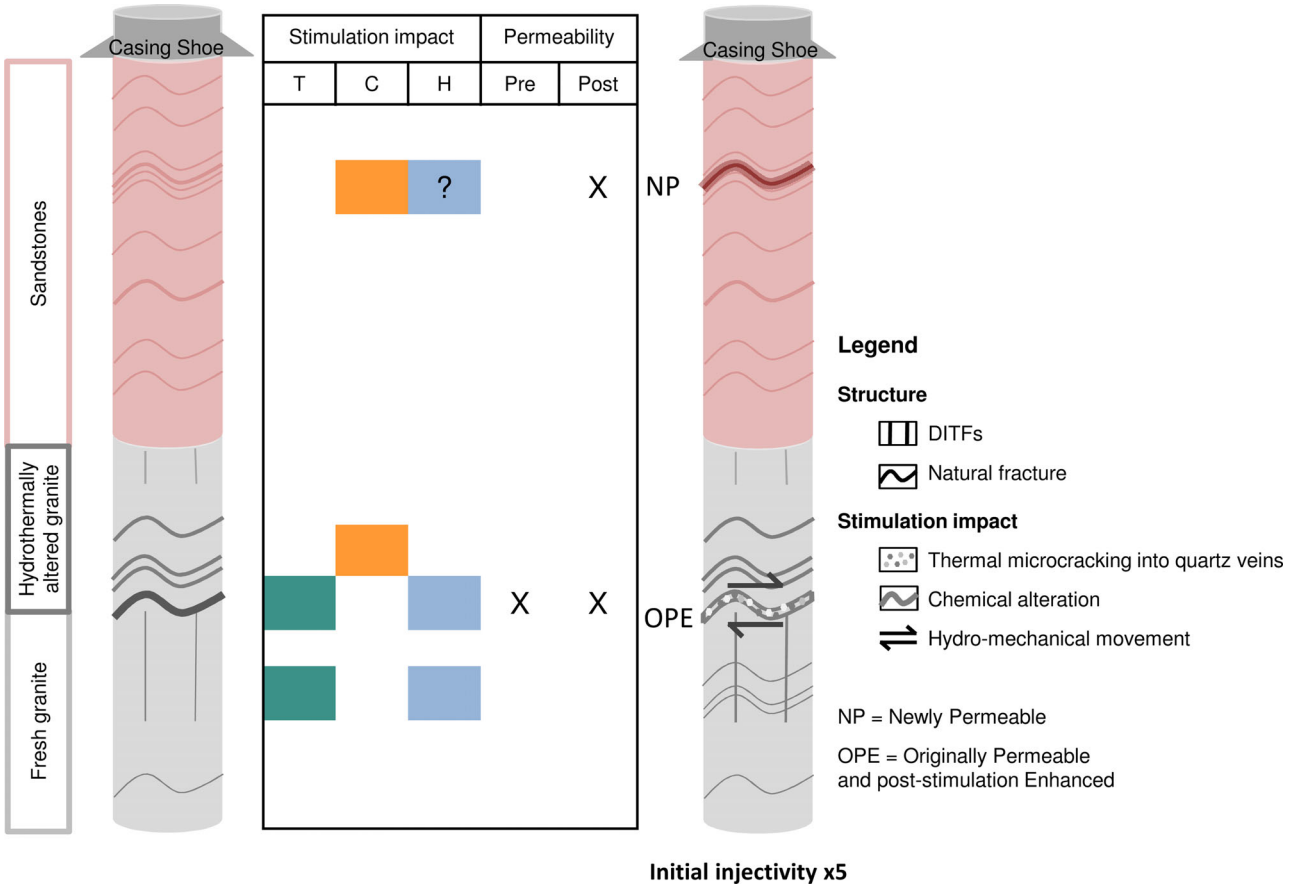

Figure 13. Schematic sketch of major modifications after the TCH stimulation of well GRT-1.

1994.5-m depth and shrinkage at the 1995.5-m depth. Erosion of fracture F2 is evident in the post-stimulation cross-section. This re-opening of fractures could be the result of mineral dissolution after the chemical stimulation or erosion at the zone of weakness at the intersection with the fracture plane highly dipping and sub-vertical to the borehole wall. Mechanical erosion of the top and the bottom of the fracture occurred with the hydraulic injection. This fracture zone is associated with a small *T* anomaly in the post-stimulation *T* log (Fig. 3), which indicates a small local post-stimulation permeability enhancement, although the contribution is minor.

Haloes of chemical alteration were also observed along isolated natural fractures in the fresh granite (Fig. 7). Tiny pre-existing fractures are clearly more visible in the fresh granite after the TCH stimulation, but thermomechanical impacts are responsible for these fracture modifications because the cold water injection was performed from the well-head and the intensity of the fracture modification decreased with depth (Fig. 13). Microcracking in the fresh granite might have occurred in the matrix, and the post-stimulation amplitude image is slightly darker locally than the pre-stimulation image (Fig. 7), whereas in the hydrothermally altered granite, the thermal microcracking occurred preferentially in quartz veins within major altered fracture zones.

The major fault zone at the 2368-m depth controls the flow rate in the well. Unfortunately, acoustic borehole imaging is not very appropriate for large diameter fluctuations associated with deep cavities, and the acoustic measurements saturated in this zone (Fig. 12). Considering the high natural injectivity of the fault, water penetrated the structure and the permeability was enhanced during the hydraulic stimulations as indicated by the *T* anomalies (Fig. 3). Hydraulic erosion during the water injection and thermal microcracking of quartz veins are associated with this permeability enhancement (Fig. 13). This fault displays a substantial offset, probably with a normal sense of motion, based on its position along the western edge of the horst. The size of the offset is difficult to estimate. Microseismicity in an area around the fault zone was recorded during the TCH stimulation. These microseismic events were localized in the crystalline basement, but they extend across an area several hectometres wide, and thus their locations are too imprecise to be attributed to this specific fault zone (Maurer *et al.* 2015). Even if the permeability enhancement is regarded as a direct consequence of the fracture reactivation, it cannot be simplistically linked to the microseismicity.

The acoustic image logs show modifications of the borehole wall resulting from the TCH stimulation of the sandstones, hydrothermally altered granite and fresh granite at a high resolution. Several tiny fractures, tensile fractures, alterations of fracture zones, and quartz veins are clearly visible in the acoustic image. These modifications would not be discernible using only *T* logs, whereas the combined post-stimulation acquisitions (*T* log and acoustic image log) allows for identification of modified zones associated with permeability enhancement.

Permeability enhancement after the TCH stimulation in well GRT-1

This comparison of pre- and post-stimulation acoustic images is a technique that is rarely performed. Slow and aseismic deformations were observed by Cornet *et al.* (1997) in well GPK-1. In the

open-hole section, several permeable altered fracture zones affect the granite. All permeable fractures and impermeable ones are critically stressed (Evans 2005). This statement implies that critical stressing is a necessary, but not a sufficient, condition for permeability development. Meller & Kohl (2014) demonstrated that on a reservoir scale, clay-rich zones foster the occurrence of aseismic movements on fractures. The permeability enhancement could be favoured by the presence of complex network of fracture partly filled by illite, secondary quartz and calcite in hydrothermalized zones. At Soultz and Rittershoffen, reservoirs are both fracture and fault dominated and stimulation operations targeted sealed fracture zones.

The open-hole section of GRT-1 is composed by sandstones and granite. The hydraulic properties of GRT-1 are controlled by the single fault of high natural permeability at the base of the altered granitic section. This permeable zone is a porous, altered and fractured zone composed by illite, quartz, calcite and sulphides. After TCH stimulation, the majority of the permeability enhancement was localized in this zone. In GRT-1, chemical stimulation attacks calcite filling fractures in sandstones and granitic basement by dissolving those minerals in a similar way. Thermal and hydraulic stimulations could more impact fracture zones in the granitic basement because no induced seismicity was observed in sandstones during and after these operations. The higher fracture permeability in the granitic basement may be explained by the fracture roughness as it was investigated at Soultz by Neuville *et al.* (2010) and also by the presence of larger damage zone around the fractures.

Zones located in sandstones at 1995-m depth, filled by carbonates and quartz, and in the deep granite in the 2396–2400-m depth interval were impacted by the chemical and thermal stimulations. They display little or no permeability enhancement. The chemical and thermal modifications increased the connectivity between the well and the near-well field, contributed to cleaning of the open-hole section after the drilling and allowed for significant effectiveness of the low-rate hydraulic stimulation, thereby minimizing the microseismicity during the operations. The hydraulic stimulation affects only the fault zone located at 2368-m depth and improves the connectivity between the well and the far-well field. During and after hydraulic stimulation, induced microseismicity is observed. After the TCH stimulations, connectivity between the well and the near-well and far-well fields are improved based on the fivefold increase in the injectivity of well GRT-1.

CONCLUSIONS

The impact of the TCH stimulation on geothermal well GRT-1 was assessed based on the comparison between the pre- and post-acoustic image logs combined with the temperature logs. Local changes observed in the acoustic images are attributed to chemical and thermo-hydro-mechanical impacts. A fracture zone in the sandstones displays surrounding chemical alteration related to mineral dissolution. The chemical modifications are associated with mechanical erosion along the tops and bottoms of the fractures subparallel to the well. A comparison of the *T* logs indicates a very small permeability enhancement. The major permeable fault zone crossing the well was not well represented in the acoustic images, but the *T* logs indicate that the initial permeability was greatly enhanced. Thermal microcracking of quartz veins and hydraulic erosion during the stimulation are probably associated with this enhancement. Below the major fault zone, in the fresh granite, a few isolated fractures were chemically altered. DITFs and small fractures were widened by the thermo-mechanical impacts on the well. The well behaviour after the TCH stimulation is controlled primarily by the fault, although almost all the natural fractures displayed evidence of modification in the acoustic logs. The *T* logs indicate significant permeability enhancement localized in and around the fault zone at the 2368-m depth.

ACKNOWLEDGEMENTS

This work was based on data from the ECOGI EGS project at Rittershoffen, France. A part of the work was performed in the framework of the LabEx G-Eau-Thermie Profonde, which is co-funded by the French government under the program ‘Investissements d’Avenir’. The manuscript was prepared as a contribution to the PhD thesis of Jeanne Vidal, co-funded by ADEME (French Agency for Environment and Energy). A part of this work was done in the framework of the H2020 DESTRESS Eu project which has received funding from the European Union Framework Programme for Research and Innovation under grant agreement No. 691728. The authors would like to kindly thank two anonymous reviewers for their contributions and manuscript improvement.

REFERENCES

Arnórsson, S., 1995. Geothermal systems in Iceland: structure and conceptual models—I. High-temperature areas, *Geothermics,* **24,** 561–602.

Axelsson, G., Thorhallsson, S. & Björnsson, G., 2006. Stimulation of geothermal wells in basaltic rock in Iceland, in *Proceedings of ENGINE Workshop 3, Stimulation of Reservoir and Microseismicity, Kartause Ittingen,* Zurich, Switzerland.

Baujard, C., Genter, A., Graff, J.-J., Maurer, V. & Dalmais, E., 2015. ECOGI, a new deep EGS project in Alsace, Rhine Graben, France, in *Proceedings of World Geothermal Congress,* Melbourne, Australia.

Baumgärtner, J. & Lerch, C., 2013. Geothermal 2.0: the Insheim Geothermal Power Plant. The second generation of geothermal power plants in the Upper Rhine Graben, in *Proceedings of Third European Geothermal Review,* Mainz, Germany.

Baumgärtner, J., Teza, D., Hettkamp, T., Homeier, G., Baria, R. & Michelet, S., 2005. Electricity production from hot rocks, in *Proceedings of World Geothermal Congress 2005,* Antalya, Turkey.

Bromley, C.J. & Majer, E.L., 2012. Geothermal induced seismicity—risks and rewards, in *Proceedings of New Zealand Geothermal Workshop,* Auckland, New Zealand.

Brudy, M. & Zoback, M.D., 1999. Drilling-induced tensile wall-fractures: implications for determination of in-situ stress orientation and magnitude, *Int. J. Rock Mech. Min. Sci.,* **36,** 191–215.

Brun, J.P., Gutscher, M.-A. & DEKORP-ECORS teams, 1992. Deep crustal structure of the Rhine Graben from DEKORP-ECORS seismic reflection data: a summary, *Tectonophysics,* **208,** 139–147.

Cornet, F.H., 1987. Results from Le Mayet de Montagne project, *Geothermics,* **16,** 355–374.

Cornet, F.H., Helm, J., Poitrenaud, H. & Etchecopar, A., 1997. Seismic and aseismic slips induced by large-scale fluid injections, *Pure appl. Geophys.,* **150,** 563–583.

Cuenot, N., Dorbath, C. & Dorbath, L., 2008. Analysis of the microseismicity induced by fluid injections at the EGS site of Soultz-sous-Forêts (Alsace, France): implications for the characterization of the geothermal reservoir properties, *Pure appl. Geophys.,* 797–828.

Davatzes, N.C. & Hickman, S.H., 2005. Comparison of acoustic and electrical image logs from the Coso Geothermal Field, CA, in *Proceedings of Thirtieth Workshop on Geothermal Reservoir Engineering,* Stanford University, Stanford, California, USA.

Dempsey, D., Kelkar, S., Davatzes, N.C., Hickman, S., Moos, D. & Zemach, E., 2014. Evaluating the roles of thermoelastic and poroelastic stress changes in the desert peak EGS stimulation, in *Proceedings of*

Thirty-Ninth Workshop on Geothermal Reservoir Engineering, Stanford University, California, USA.

Dezayes, C., Genter, A. & Valley, B., 2010. Structure of the low permeable naturally fractured geothermal reservoir at Soultz, *C. R. Geosci.,* **342,** 517–530.

Dezayes, C., Sanjuan, B., Gal, F. & Lerouge, C., 2014. Fluid geochemistry monitoring and fractured zones characterization in the GRT1 borehole (ECOGI project, Rittershoffen, Alsace, France), in *Proceedings of Deep Geothermal Days,* Paris, France.

Economides, M.J. & Nolte, K.G., 1989. *Reservoir Stimulation,* 2nd edn, Prentice Hall.

Evans, K.F., 2005. Permeability creation and damage due to massive fluid injections into granite at 3.5 km at Soultz: 2. Critical stress and fracture strength, *J. geophys. Res.,* **110**, doi:10.1029/2004JB003168.

Evans, K., Genter, A. & Sausse, J., 2005a. Permeability creation and damage due to massive fluid injections into granite at 3.5 km at Soultz: 1. Borehole observations, *J. geophys. Res.,* **110**, doi:10.1029/2004JB003168.

Evans, K. *et al.*, 2005b. Microseismicity and permeability enhancement of hydrogeologic structures during massive fluid injections into granite at 3 km depth at the Soultz HDR site, *Geophys. J. Int.,* **160,** 389–412.

Genter, A., Traineau, H., Ledésert, B., Bourgine, B. & Gentier, S., 2000. Over 10 years of geological investigations within the HDR Soultz project, France, in *Proceedings of World Geothermal Congress 2000,* Kyushu - Tohoku, Japan.

Grant, A.M., Clearwater, J., Quinão, J., Bixley, F.P. & Le Brun, M., 2013. Thermal stimulation of geothermal wells: a review of field data, in *Proceedings of Thirty-Eighth Workshop on Geothermal Reservoir Engineering,* Stanford University, Stanford, California, USA.

Griffiths, L., Heap, M.J., Reuschlé, T., Baud, P. & Schmittbuhl, J., 2015. Permeability enhancement by shock cooling, in *Proceedings of European Geosciences Union*, *Geophysical Reasearch Abstracts,* Vienna, Austria.

Guillou-Frottier, L., 2003. Compilation et analyse des données thermiques sur le champ géothermique de Bouillante (Rapport final No. RP-52452-FR), *BRGM*.

Guillou-Frottier, L. & Jaupard, C., 1995. On the effect of continents on mantle convection, *J. geophys. Res.,* **110,** 24 217–24 238.

Häring, M.O., Schanz, U., Ladner, F. & Dyer, B.C., 2008. Characterisation of the Basel 1 enhanced geothermal system, *Geothermics,* **37,** 469–495.

Hettkamp, T., Baumgärtner, J., Teza, D. & Lerch, C., 2013. Experiences from 5 years operation in Landau, in *Proceedings of Third European Geothermal Review,* Mainz, Germany.

Hosni, A., Gentier, S., Genter, A., Riss, J., Billaux, D. & Dedecker, F., 2003. Coupled THM modeling of stimulated permeable fractures in the near well at the Soultz-sous-Forêts site (France), in *Proceedings of GeoProc 2003: International Conference on Coupled T-H-M-C Processec in Geosystems,* Stockholm, Sweden.

Huenges, E., Holl, H.-G., Bruhn, D., Brandt, W., Saadat, A., Moeck, I. & Zimmermann, G., 2007. Current state of the EGS project Gross Schönebeck - Drilling into deep sedimentary geothermal reservoirs, in *Proceedings of European Geothermal Congress,* Szeged, Hungary.

Ikeuchi, K., Doi, N., Sakagawa, Y., Kamenosono, H. & Uchida, T., 1998. High-temperature measurements in well WD-1A and the thermal structure of the kakkonda geothermal system, Japan, *Geothermics,* **27,** 591–607.

Illies, H.J., 1972. The Rhine graben rift system-plate tectonics and transform faulting, *Geophys. Surv.,* **1,** 27–60.

Illies, H.J., 1975. Recent and paleo-intraplate tectonics in stable Europe and the Rhinegraben rift system, *Tectonophysics,* **29,** 251–264.

Kappelmeyer, O., Gérard, A., Schloemer, R., Ferrandes, F., Rummel, F. & Benderitter, Y., 1992. European HDR project at Soultz-sous-Forêts: general presentation, in *Geothermal Energy in Europe - The Soultz Hot Dry Rock Project,* ed. Bresee, J.C., Grodon and Breach Science Publishers S.A.

Magnenet, V., Fond, C., Genter, A. & Schmittbuhl, J., 2014. Two-dimensional THM modelling of the large scale natural hydrothermal circulation at Soultz-sous-Forêts, *Geotherm. Energy,* **2,** 17, doi:10.1186/s40517-014-0017-x.

Majer, E.L., Baria, R., Stark, M., Oates, S., Bommer, J., Smith, B. & Asanuma, H., 2007. Induced seismicity associated with Enhanced Geothermal Systems, *Geothermics,* **36,** 185–222.

Maurer, V., Cuenot, N., Gaucher, E., Grunberg, M., Vergne, J., Wodling, H., Lehujeur, M. & Schmittbuhl, J., 2015. Seismic monitoring of the Rittershoffen EGS project (Alsace, France), in *Proceedings of World Geothermal Congress 2015,* Melbourne, Australia.

Meller, C. & Kohl, T., 2014. The significance of hydrothermal alteration zones for the mechanical behavior of a geothermal reservoir, *Geotherm. Energy,* **2,** 1–21.

Meller, C., Kontny, A. & Kohl, T., 2014. Identification and characterization of hydrothermally altered zones in granite by combining synthetic clay content logs with magnetic mineralogical investigations of drilled rock cuttings, *Geophys. J. Int.,* **199,** 465–479.

Ménillet, F., Durand, M., Genter, A. & Party, J.-P., 2015. Notice explicative, Carte géologique de la France (1/50000), feuille Haguenau. BRGM, Orléans, France, p. 345.

Mukuhira, Y., Asanuma, H., Niitsuma, H. & Häring, M.O., 2013. Characteristics of large-magnitude microseismic events recorded during and after stimulation of a geothermal reservoir at Basel, Switzerland, *Geothermics,* **45,** 1–17.

Nami, P., Schellschmidt, R., Schindler, M. & Tischner, T., 2008. Chemical Stimulation operations for reservoir development of the deep crystalline HDR/EGS system at Soultz-sous-Forêts (France), in *Proceedings of Thirty-Second Workshop on Geothermal Reservoir Engineering,* Stanford University, California, USA, p. 5.

Neuville, A., Toussaint, R. & Schmittbuhl, J., 2010. Fracture roughness and thermal exchange: A case study at soultz-sous-forêts, *C.R. Geosci.,* **342,** 616–625.

Pine, R.J. & Batchelor, A.S., 1984. Downward migration of shearing in jointed rock during hydraulic injections, *Int. J. Rock Mech. Min. Sci. Geomech. Abstr.,* **21,** 249–263.

Portier, S., Vuataz, F.-D., Nami, P., Sanjuan, B. & Gérard, A., 2009. Chemical stimulation techniques for geothermal wells: experiments on the three-well EGS system at Soultz-sous-Forêts, *France*, *Geothermics,* **38,** 349–359.

Ratouis, T.M.P. & Zarrouk, S.J., 2016. Factors controlling large-scale hydrodynamic convection in the Taupo Volcanic Zone (TVZ), New Zealand, *Geothermics*, **59**(Part B), 236–251.

Recalde Lummer, N., Rauf, O., Gerdes, S., Genter, A., Scheiber, J. & Villadangos, G., 2014. New biodegradable stimulation system - First field trial in granite/Bunter sandstone formation for a geothermal application in the Upper Rhine Valley, in *Proceedings of Deep Geothermal Days,* Paris, France.

Rose, P., Xu, T., Kovac, K., Mella, M. & Pruess, K., 2007. Chemical stimulation in near-wellbore geothermal formations: silica dissolution in the presence of calcite at high temperature and high pH, *Presented at the Proceedings of Thirty-Second Workshop on Geothermal Reservoir Engineering,* Stanford University, California.

Schindler, M. *et al.*, 2010. Successful hydraulic stimulation techniques for electric power production in the Upper Rhine Graben, Central Europe, in *Proceedings of World Geothermal Congress 2010,* Bali, Indonesia.

Schmittbuhl, J., Lengline, O., Cornet, F., Cuenot, N. & Genter, A., 2014. Induced seismicity in EGS reservoir: the creep route, *Geotherm. Energy,* **2,** 14, doi:10.1186/s40517-014-0014-0.

Schulte, T., Zimmermann, G., Vuataz, F.-D., Portier, S., Tischner, T., Junker, R., Jatho, R. & Huenges, E., 2010. Enhancing Geothermal Reservoirs, in *Geothermal Energy Systems - Exploration, Development, and Utilization,* Wiley-VCH Verlag GmbH & Co. KGaA.

Serra, O., 2008. *The Well Logging Handbook,* Editions Technip.

Tingay, M., Reinecker, J. & Müller, B., 2008. Borehole breakout and drilling induced fracture analysis from image logs, *World Stress Map Project Stress Analysis Guidelines,* http://www.world-stress-map.org

Traineau, H., Genter, A., Cautru, J.-P., Fabriol, H. & Chèvremont, P., 1992. Petrography of the Granite Massiffrom Drill Cutting Analysis and Well Log Interpretation in the Geothermal HDR Borehole GPK-1 (Soultz, Alsace, France), in *Geothermal Energy in Europe - The Soultz Hot Dry*

Rock Project, ed. Bresee, J.C., Gordon and Breach Science Publishers S.A.

Tulinius, H., Correia, H. & Sigurdsson, O., 2000. Stimulating a high enthalpy well by thermal cracking, *Presented at the Proceedings World Geothermal Congress,* Kyushu - Tohoku, Japan.

Valley, B.C. & Evans, K.F., 2007. Stress state at Soultz-sous-Forêts to 5 km depth from wellbore failure and hydraulic observations, in *Proceedings of Thirty-Second Workshop on Geothermal Reservoir Engineering,* Stanford University, Stanford, California, USA.

Vidal, J., Genter, A. & Schmittbuhl, J., 2015. How do permeable fractures in the Triassic sediments of Northern Alsace characterize the top of hydrothermal convective cells? Evidence from Soultz Geothermal boreholes (France), *Geotherm. Energy,* **3,** doi:10.1186/s40517-015-0026-4

Villemin, T. & Bergerat, F., 1987. L'évolution structurale du fosse rhénan au cours du Cénozoïque: un bilan de la déformation et des effets thermiques de l'extension, *Bulletin de la Société Géologique de France,* **8,** 245–255.

Zemaneck, J., Glen, E.E.J., Norton, L.J. & Cardwell, R.L., 1970. Formation evaluation by inspection with the borehole televiewer, *Geophysics,* **35,** 254–269.

Ziegler, P.A., 1992. European Cenozoic rift system, *Tectonophysics,* **208,** 91–111.